ACS APPLIED MATERIALS & INTERFACES

Research Article

Cite This: ACS Appl. Mater. Interfaces 2019, 11, 30053−30064

www.acsami.org

Simultaneous Tailoring of Dual-Phase Fluoride Precipitation and Dopant Distribution in Glass to Control Upconverting Luminescence

Daqin Chen,*[,†,∥] Yongzhao Peng,[‡,∥] Xinyue Li,[‡] Jiasong Zhong,[‡] Hai Huang,[†,§] and Jiangkun Chen[†,§]

[†]College of Physics and Energy, Fujian Normal University, Fuzhou, Fujian 350117, China

[‡]College of Materials & Environmental Engineering, Hangzhou Dianzi University, Hangzhou, Zhejiang 310018, China

[§]Fujian Provincial Collaborative Innovation Center for Optoelectronic Semiconductors and Efficient Devices, Xiamen, Fujian 361005, China

Supporting Information

ABSTRACT: In situ glass crystallization is an effective strategy to integrate lanthanide-doped upconversion nanocrystals into amorphous glass, leading to new hybrid materials and offering an unexploited way to study light−particle interactions. However, the precipitation of Sc^{3+}-based nanocrystals from glass is rarely reported and the incorporation of lanthanide activators into the Sc^{3+}-based crystalline lattice is formidably difficult owing to their large radius mismatch. Herein, it is demonstrated that lanthanide dopants with smaller ionic radii can act as nucleating agents to promote the nucleation/growth of KSc_2F_7 nanocrystals in oxyfluoride aluminosilicate glass. A series of structural and spectroscopic characterizations indicate that Ln-dopant-induced K/Sc/Ln/F amorphous phase separation from glass is an essential prerequisite for the precipitation of KSc_2F_7 and the partition of Ln dopants into the KSc_2F_7 lattice by substituting Sc^{3+} ions. Importantly, modifying the Ln-to-Sc ratio in glass enables to control competitive crystallization of KSc_2F_7 and Ln-based (KYb_2F_7, KLu_2F_7, and KYF_4) nanocrystals and produce dual-phase fluoride-embedded nanocomposites with distinct crystal fields. Consequently, tunable multicolor upconversion luminescence can be achieved through diversified regulatory approaches, such as adjustment of the dual-phase ratio, selective separation of Ln^{3+} dopants, and alteration of incident pumping laser. As a proof-of-concept experiment, the application of dual-phase glass as a color converter in 980 nm laser-driven upconverting lighting is demonstrated.

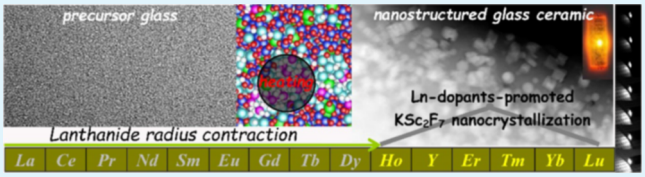

KEYWORDS: *upconversion, glass ceramics, KSc_2F_7, lanthanide, luminescence*

1. INTRODUCTION

Lanthanide (Ln^{3+})-doped upconversion (UC) luminescent materials, enabling to convert low-energy incident laser into high-energy photons via a multiphoton absorption process, have been extensively explored to apply in optoelectronic fields,[1,2] and especially, Ln-doped UC nanocrystals (UCNCs) have received considerable attention for their promising applications in bioimaging, anticounterfeiting, therapy, and display.[3−11] Generally, UC efficiency and spectral profile are highly correlated to hosts where Ln^{3+} activators reside. Among various host materials, rare earth (RE) fluorides have been widely employed because of their intrinsically low phonon energy, relatively high chemical stability, and easy incorporation of Ln^{3+} dopants.[12−17] For instance, hexagonal β-$NaREF_4$ (RE = Y, Gd, Lu) doped with Er^{3+} or Tm^{3+}, commonly combined with Yb^{3+} as a sensitizer, have been regarded as one of the most efficient green or blue UC materials.[18−20] To achieve multicolor and high-efficient UC luminescence, layer-by-layer core−shell nanostructures have been deliberately designed to spatially separate Ln^{3+} dopants in different layers and effectively eliminate the deleterious cross relaxations among different Ln^{3+} activators.[21]

In addition to optoelectronic applications of UCNCs in nanoscale, there is a growing necessity to integrate them with a bulk photonic platform to manipulate their excellent optical properties and offer a previously unexploited way to investigate light−NCs interactions in photonic devices. Glass is a desirable bulk medium to disperse UCNCs for its facile synthesis, high transparency, high stability, and the ability to be shaped into various shapes. Recently, direct incorporation of the presynthesized UCNCs into a low-melting glass to produce a hybrid photonic material via cosintering has been reported.[22,23] Unfortunately, this strategy merely enables to introduce UCNCs with large size (several hundreds of nanometers) into glass to avoid their decomposition by high-temperature melting and dope low-content UCNCs to prevent adverse light scattering and high optical loss. As an alternative, in situ glass crystallization has been widely adopted to integrate Ln-containing UCNCs in glass (the so-called nanostructured glass ceramic, NGC), which highly relies on elaborate design of the glass network and appropriate control of nucleation/

Received: July 1, 2019
Accepted: July 31, 2019
Published: July 31, 2019

DOI: 10.1021/acsami.9b11516
ACS Appl. Mater. Interfaces 2019, 11, 30053−30064

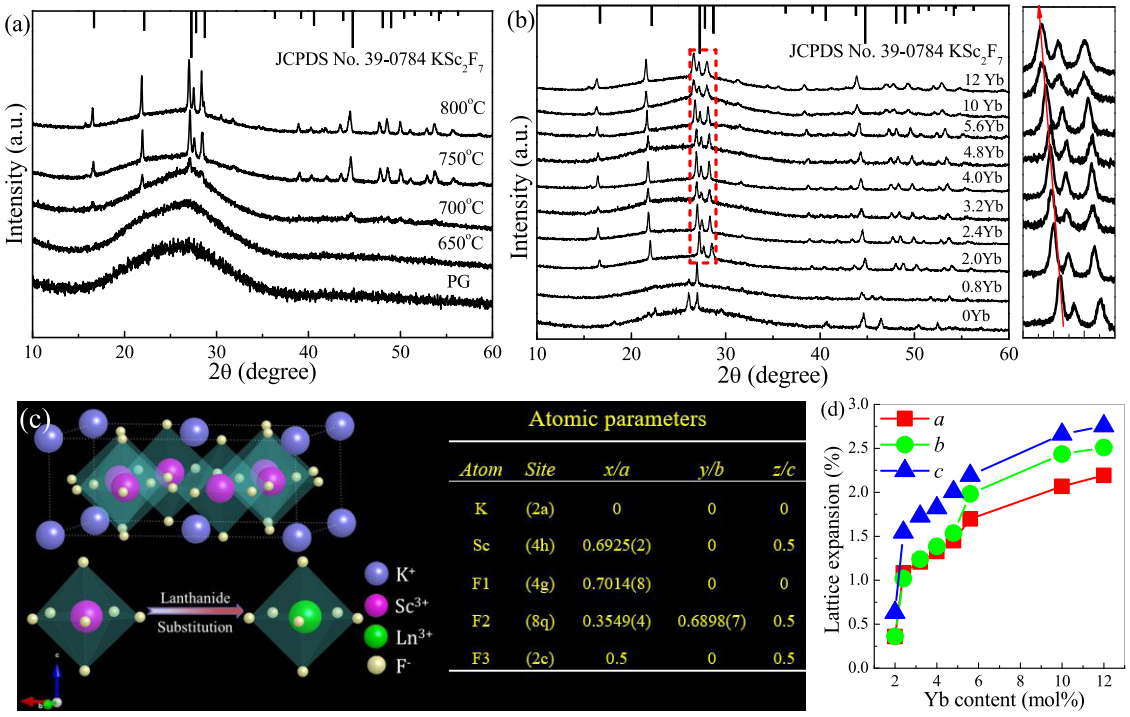

Figure 1. XRD patterns of the as-prepared products: (a) Yb-doped PG and NGCs obtained by heating PG at different temperatures, (b) NGCs doped with different Yb^{3+} concentrations. Enlarged XRD patterns of (b) show that diffraction peaks shift toward lower angles with the increase of Yb^{3+} content. (c) Schematic illustration of the crystal structure and crystallographic data of orthorhombic KSc_2F_7, where the doping of Ln^{3+} ions will substitute Sc^{3+} ones. (d) Lattice expansion degree for unit cell parameters (*a*, *b*, *c*) of KSc_2F_7 NCs versus Yb^{3+} doping content.

growth (or precipitation) of fluoride NCs from the glass matrix.[24,25] In this method, a critical point is to achieve the growth of a specific fluoride phase and more importantly facilitate the diffusion of Ln^{3+} dopants from glass into the precipitated crystalline lattice through heating glass above the glass transition temperature. So far, several Ln-doped RE fluoride UCNC (such as $NaYF_4$)-embedded NGCs have been fabricated and exhibited outstanding optical performance.[26−32] Notably, different to the cases of wet-chemical synthesis, the growth of core/shell UCNCs in amorphous glasses is hard owing to the limited growth space for precipitations in glass network interstitial sites as well as the impeding role of the solid glass network in ionic diffusion. As an alternative, simultaneous precipitation of multiphase nanoparticles in the glasses may be an effective solution to enable spatial separation of doping activators. Indeed, simultaneous crystallization of fluoride (LaF_3, YF_3, and GdF_3) and oxide (Ga_2O_3, $ZnAl_2O_4$) NCs in glasses has been achieved and Ln^{3+} dopants and transition metal ions (Ni^{2+}, Cr^{3+}) can be separately partitioned into fluoride and oxide crystals, respectively.[32−35]

Up to now, there is no report concerning the precipitation of distinct dual-phase fluorides and the controlling of Ln^{3+} dopant distribution in glass. Generally, the precipitated fluorides in glass should enable the incorporation of Ln^{3+} dopants, which limits the crystallized fluorides to be rare earth fluorides (such as LaF_3, $LiYbF_4$, $NaLaF_4$, and KLu_2F_7)[36−39] and alkaline earth fluorides (such as CaF_2, SrF_2, and BaF_2).[40] Unfortunately, simultaneous crystallization of rare earth fluorides and alkaline earth fluorides is formidably difficult in glasses. Instead, it was usually reported that the precipitation phases were alkaline earth and rare earth compounds such as Ba_2LaF_7 and $SrYb_2F_7$.[28,41]

Scandium with electron configuration of $1s^22s^22p^63s^23p^63d^14s^2$ is located at the top of group IIIB in the periodic table and is historically classified as an RE element. Notably, the distinct electron configuration and small ionic radius of Sc^{3+} relative to traditional RE ions may lead to different UC emitting behaviors in Ln-doped scandium-based fluorides. For example, Yb/Er-doped Na_xScF_{3+x} UCNCs have been recently reported to yield much higher red-to-green UC ratio than that in Yb/Er/*β*-$NaYF_4$.[42] Recently, we have successfully realized the precipitation of Na_3ScF_6 NCs from glass.[43] Unfortunately, Ln^{3+} dopants in this glass system prefer to self-crystallization rather than partition into the Na_3ScF_6 crystalline lattice,[43] probably owing to large ionic radius mismatch (13−34%) between Sc^{3+} and Ln^{3+} (Table S1). This result indicates the possibility of coprecipitation of dual-phase Sc-based and RE-based fluorides in the same glass matrix. One of the key steps is to enable selective incorporation of specific Ln^{3+} dopants in these two kinds of fluoride crystals to control dopant distribution. In this work, we report the controllable crystallization of KSc_2F_7 NCs from aluminosilicate glass for the first time, where Ln^{3+} dopants (such as Er, Tm, and Yb) with small ionic radii can selectively separate from the glass matrix into the KSc_2F_7 crystalline lattice. Importantly, modifying the Ln-to-Sc ratio in glass enables to control competitive crystallization of KSc_2F_7 and RE-based (KYb_2F_7, KLu_2F_7, KYF_4) nanocrystals and elaborately tune multicolor upconversion luminescence of Ln^{3+} dopants for its distinct dual-phase crystal-field environments. To the best of our knowledge, this is the first report on the fabrication of Ln^{3+}-doped Sc-based fluoride NC-contained NGCs via in situ glass crystallization and the related UC optical properties have not been reported to date.

DOI: 10.1021/acsami.9b11516
ACS Appl. Mater. Interfaces 2019, 11, 30053−30064

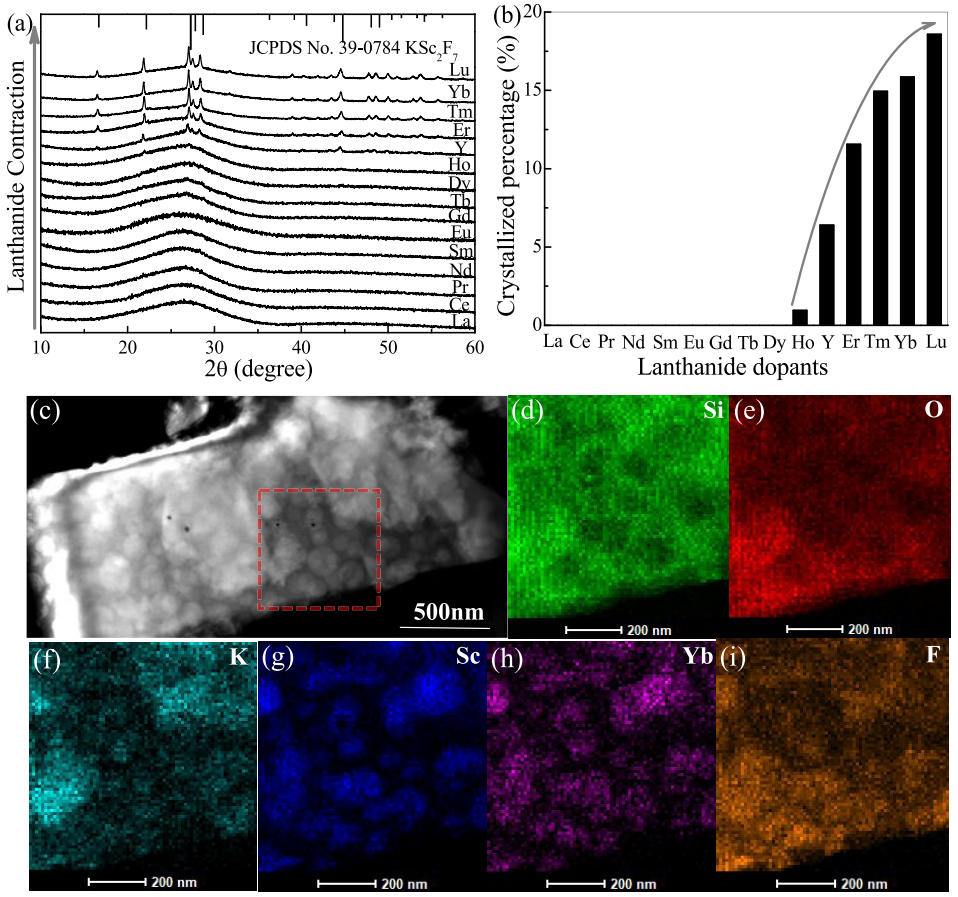

Figure 2. (a) XRD patterns of NGCs containing Ln^{3+} dopants (Ln = La−Lu). (b) Crystallized volume percentage of KSc_2F_7 NCs versus Ln^{3+} dopants. (c) STEM image of a typical Yb-doped NGC and the related elemental mapping of (d) Si, (e) O, (f) K, (g) Sc, (h) Yb, and (i) F.

2. EXPERIMENTAL SECTION

2.1. Fabrication of Nanostructured Glass Ceramics (NGCs). The NGCs were prepared by high-temperature melt-quenching and subsequent heat treatment. High-purity raw materials of about 14 g were thoroughly mixed and melted in a covered alumina crucible inside a muffle furnace at 1500 °C for 30 min in an air atmosphere to produce a homogeneous melting. Then, the melt was poured into a 300 °C brass copper mold to produce precursor glass (PG). Finally, the obtained glasses were crystallized by heat treatment at 650−850 °C for 2 h to induce fluoride crystallization in the glass matrix to achieve NGCs.

2.2. Structural Characterizations. X-ray diffraction (XRD) analysis was carried out to identify the precipitated phases in glass using a powder diffractometer (MiniFlex600 RIGAKU) with Cu Kα radiation (λ = 0.154 nm) operating at 40 kV. The crystallization percentage was determined based on the ratio of the integrated area of the crystalline diffraction peaks to the total XRD pattern. Fourier transform infrared (FTIR) spectra were measured via a PerkinElmer IR spectrometer using the KBr pellet technique. Raman spectra were determined by a LabRam HR Raman spectrometer operated with a 532 nm laser as the excitation source. Microstructure observations of NGCs were carried out on a JEOL JEM-2010 TEM operating at 200 kV accelerating voltage. Scanning transmission electron microscopy (STEM) images were taken on a FEI aberration-corrected Titan Cubed S-Twin transmission electron microscope operating in a high-angle annular dark-field (HAADF) mode. ^{28}Si, ^{45}Sc, ^{19}F, and ^{27}Al magic angle spinning (MAS) nuclear magnetic resonance (NMR) spectra were performed using a Bruker Instruments ADVANCE III HD 400.

2.3. Optical Characterizations. Photoluminescence (PL), UC emission spectra, and time-resolved spectra were recorded on an Edinburgh Instruments FS5 spectrofluorometer equipped with 150 W xenon lamps, 60 W pulse xenon lamps, and a 980 nm diode laser as the excitation sources. UC decay lifetimes were determined via equation $\tau = \int I(t)\,dt/I_0$, where $I(t)$ is the time-related luminescence intensity and I_0 is the peak intensity. Temperature-dependent UC spectra were measured on an Edinburgh Instruments FLS980 spectrofluoremeter equipped with a Linkam THMS600 temperature-controlling stage. The optoelectronic parameters for the GC-based UC solid-state lighting, including luminous flux, radiant flux, color rendering index (CRI), correlated color temperature (CCT), luminous efficiency (LE), energy efficiency, and Commission Internationale de L'Eclairage (CIE) color coordinates, were measured in a transmissive configuration by a sphere spectroradiometer system consisting of a high-power 980 laser source (MDL-III-980-3W, CNI, China), an integrating sphere (30 cm in diameter, Labsphere Inc.), and a charge-coupled device spectrometer (CDS2100, Labsphere Inc.).

3. RESULTS AND DISCUSSION

3.1. Precipitation of Single-Phase KSc_2F_7 NCs in Glass. An appropriate design of glass composition and network structure is an essential prerequisite for in situ nucleation/growth of specific fluoride NCs among glass. Herein, Yb-doped precursor glass (PG) of SiO_2−Al_2O_3−K_2CO_3−KF−ScF_3−YbF_3 was prepared by a melt-quenching method. Typical amorphous humps are observed in the XRD pattern of PG, and distinct diffraction peaks assigned to orthorhombic KSc_2F_7 phase (JCPDS no. 39-0784) appear after glass crystallization at 700−800 °C for 2 h (Figure 1a). In contrast, without Yb^{3+} dopants, the diffraction peaks are totally different from those of the KSc_2F_7 phase (Figure S1),

DOI: 10.1021/acsami.9b11516
ACS Appl. Mater. Interfaces 2019, 11, 30053−30064

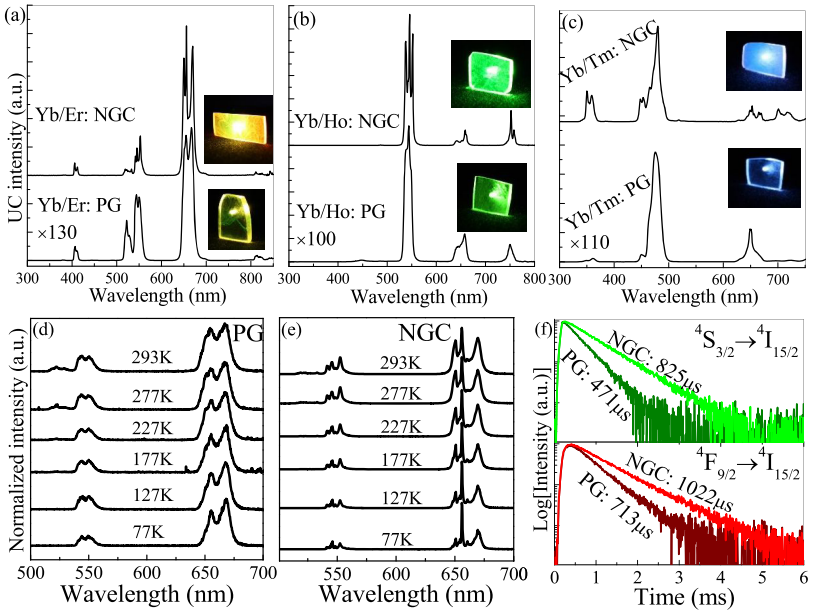

Figure 3. UC emission spectra (λ_{ex} = 980 nm) of Yb/Ln-doped PG and the corresponding NGC samples: (a) Ln = Er, (b) Ln = Ho, and (c) Ln = Tm. Insets are the corresponding UC luminescence photographs of PGs and NGCs under irradiation of 980 nm laser. Temperature-dependent (77−293 K) UC emission spectra of (d) Yb/Er-doped PG and (e) NGC. (f) Time-resolved UC spectra of PG and NGC by monitoring Er^{3+} green and red emission spectra.

indicating Yb^{3+}-doping-induced nucleation/growth of KSc_2F_7 crystals in this glass system. To better unravel the role of Yb^{3+} dopants, XRD patterns of a series of NGCs doped with various Yb^{3+} contents are shown in Figure 1b. Notably, the precipitation of the KSc_2F_7 phase in glass can occur only after the Yb^{3+} doping content reaches a critical value (2 mol %). In addition, the diffraction peaks gradually shift toward lower angles with the increase of Yb^{3+} content owing to the substitution of Sc^{3+} ions by larger Yb^{3+} ones. There is one scandium site, one potassium site, and three bridging fluorine sites in the crystal structure of orthorhombic KSc_2F_7 (Figure 1c). The edge- and corner-linked continuous chains of ScF_7 pentagonal bipyramids form sheets in the *ab* plane, which are further linked apically into a three-dimensional structure.[44] Compared to the values without Yb^{3+} doping, the evaluated unit cell parameters (*a*, *b*, *c*) for Yb^{3+}-doped samples indeed indicate the lattice expansion, as shown in Figure 1d. Therefore, it is concluded that Yb^{3+} dopants act as nucleating agents to promote the nucleation/growth of the KSc_2F_7 phase in glass, which enables its partition into the KSc_2F_7 crystalline lattice by substituting Sc^{3+} site.

In a further experiment, the family of Ln^{3+} from La^{3+} to Lu^{3+}, including Y^{3+}, was each introduced into glass with a doping content of 2 mol %, as shown in Figure 2a. The Ln^{3+} ionic radius gradually decreases from La^{3+} (r = 1.19 Å) to Lu^{3+} (r = 1.00 Å) owing to the effect of lanthanide contraction (Table S1). Interestingly, not any crystallized phase in glass is detected when the ionic radii of Ln^{3+} dopants (Ln = La, Ce, Pr, Nd, Sm, Eu, Gd, Tb, and Dy) are large and the orthorhombic KSc_2F_7 NCs can be precipitated from the glass matrix only for specific Ln^{3+} (Ln = Ho, Y, Er, Tm, Yb, and Lu) dopants with smaller ionic radii. Notably, the crystallized fraction of KSc_2F_7 NCs in glass gradually enhances with the decrease of Ln^{3+} radius (Figure 2b), which means that the smaller the size of Ln^{3+} dopants, the easier the nucleation/growth of KSc_2F_7 NCs in glass. The HAADF−STEM image (Figure 2c) distinctly discerns the contrast for KSc_2F_7 (bright) and aluminosilicate glass matrix (dark) due to the large difference of atomic number between K/Sc (Z = 19/21) and Al/Si (Z = 14/13). TEM and high-resolution TEM (HRTEM) micrographs further indicate that KSc_2F_7 NCs with high crystallinity and well-resolved lattice fringes homogeneously distribute inside the glass matrix (Figure S2). Elemental mappings show the segregation of K, Sc, and F elements in the Si/O glass matrix (Figure 2d−i). Importantly, the distribution of Yb element is totally the same as that of Sc one (Figure 2g,h), certainly verifying the incorporation of Yb dopants into KSc_2F_7 NCs.

3.2. Selective Separation of Ln^{3+}-Emitting Centers in KSc_2F_7 Lattice. UC emission spectra of Yb/Ln (Ln = Er, Ho, or Tm)-doped PGs and NGCs were recorded to unveil the location of Ln^{3+} dopants in the nanocomposites, as shown in Figure 3a−c. Characteristic Er^{3+} violet ($^2H_{9/2} \rightarrow {}^4I_{15/2}$), green ($^2H_{11/2}$,$^4S_{3/2} \rightarrow {}^4I_{15/2}$), and red ($^4F_{9/2} \rightarrow {}^4I_{15/2}$); Ho^{3+} green ($^5S_2$,$^5F_4 \rightarrow {}^5I_8$), red ($^5F_5 \rightarrow {}^5I_8$), and near-infrared ($^5I_4 \rightarrow {}^5I_8$); and Tm^{3+} ultraviolet ($^1D_2 \rightarrow {}^3H_6$), blue ($^1G_4 \rightarrow {}^3H_6$, $^1D_2 \rightarrow {}^3F_4$), and red ($^5F_{2,3} \rightarrow {}^3H_6$) UC emission spectra are observed for both PG and NGC samples. The related energy transfer multiphoton UC processes are illustrated in Figure S3. Notably, the UC intensities of NGCs are about 100 times higher than those of PGs and obvious intensified UC luminescence for NGCs are observed (insets of Figure 3a−c), indicating the alteration of Ln^{3+} ligand fields after glass crystallization. The UC quantum yields for the Yb/Er-, Yb/Ho-, and Yb/Tm-doped KSc_2F_7 NGCs are determined to be 0.39, 0.044, and 0.017%, respectively.

Taking Er^{3+} dopants as a typical structural probe, temperature-dependent Er^{3+} UC emission spectra were further measured to trace the variation of a Er^{3+} local environment after glass crystallization. Both green and red UC emission spectra of Er^{3+} show typical glasslike inhomogeneous broadening for PG even after the recording temprature cools down to 77 K (Figure 3d), and they become narrow and Stark-splitting for NGC (Figure 3e). All of these results can be

DOI: 10.1021/acsami.9b11516
ACS Appl. Mater. Interfaces 2019, 11, 30053−30064

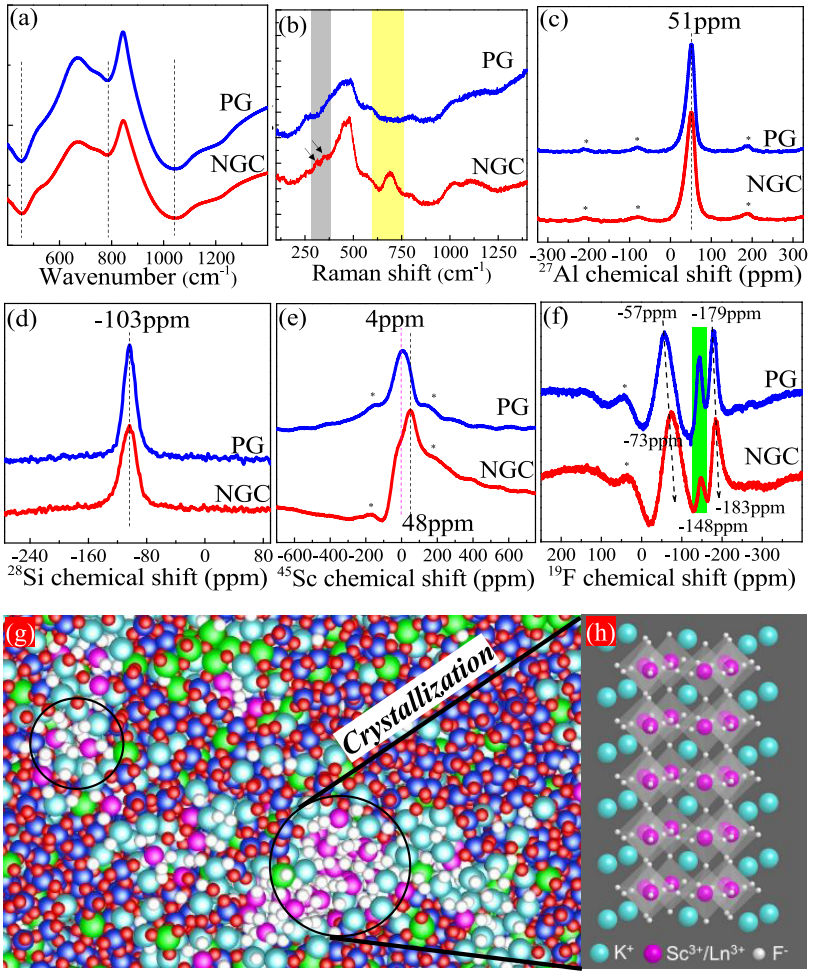

Figure 4. (a) FTIR spectra; (b) Raman spectra (λ_{ex} = 532 nm); and (c–f) ^{27}Al, ^{28}Si, ^{45}Sc, ^{19}F NMR spectra at a spinning frequency of 14 kHz for the precursor glass and the corresponding NGC; (*) represents spin sidebands. (g) Schematic illustration of the glass network structure and K/Sc/Ln/F amorphous segregation (black circle regions) in the glass matrix (Si, blue; Al, green; O, red; K, cyan; F, white; and Sc/Ln, pink spheres) and (h) crystallized Ln-doped KSc_2F_7 crystal.

attributed to the incorporation of Ln^{3+} (Ln = Er, Ho, or Tm) dopants into the KSc_2F_7 crystalline lattice with low phonon energy, leading to the production of crystallike UC luminescence and reduction of nonradiative relaxation of Ln^{3+}. Evidently, time-resolved UC spectra by monitoring Er^{3+} $^4S_{3/2}$, $^4F_{9/2}$ (Figure 3f); Ho^{3+} $^5S_2$,$^5F_4$ (Figure S4a); and Tm^{3+} $^1G_4$ (Figure S4b) emitting states verify remarkably elongated Er^{3+}, Ho^{3+}, and Tm^{3+} UC decay lifetimes after glass crystallization.

As a comparison, no obvious change is found in photoluminescence (PL) spectra and decay curves of other Ln^{3+} (Ln = Ce, Pr, Nd, Sm, Eu, Gd, Tb, Dy)-doped PG and NGC samples (Figures S5 and S6), indicating that these Ln^{3+} dopants are difficult to enter in the KSc_2F_7 lattice by substituting Sc^{3+} ions. This is reasonable by considering the large radius mismatch (18–33.7%, Table S1) between Ln^{3+} (Ln = Dy–Ce, 1.05–1.19 Å) and Sc^{3+} (0.89 Å), being consistent with XRD results (Figure 2a). All of these results confirm that Ln^{3+} dopants with smaller ionic radii (Ln = Ho, Y, Er, Tm, Yb, Lu) can selectively separate from the glass matrix into the KSc_2F_7 crystalline lattice after glass crystallization (heat treatment). Consequently, it is believed that the present KSc_2F_7 NC-embedded glass is a suitable UC host since Yb sensitizers and Ho-, Er-, and Tm-emitting centers can be well incorporated into the low-phonon-energy KSc_2F_7 crystalline lattice.

3.3. Glass Network Structure and Dual-Phase Coprecipitation. A series of structural characterizations were carried out to get information about the glass network structure. Fourier transform infrared (FTIR) spectra (Figure 4a) show antisymmetric stretching vibrations of Si–O–Si and Si–O–Al bonds (1000–1200 cm^{-1}), symmetric stretching modes with intertetrahedral vibrations of Si–O–Si and Al–O–Al units (~780 cm^{-1}), and bending vibrational modes of Si–O–Si and Si–O–Al bonds (~450 cm^{-1}),[45] indicating that the glass network consists of [SiO_4] and [AlO_4] tetrahedra. Raman spectra of PG and NGC (Figure 4b) can be divided into two separated regions, high-frequency vibrational bands (400–1200 cm^{-1}) of [SiO_4] and [AlO_4] groups[27] and two narrow low-frequency vibrational peaks (300–400 cm^{-1}) of orthorhombic KSc_2F_7 NCs. Additionally, an extra Raman peak (~720 cm^{-1}) assigned to [AlO_6] octahedral vibration appears after glass crystallization, indicating that the glass network structure tends to be broken and overall crystallized. ^{27}Al and ^{28}Si nuclear magnetic resonance (NMR) spectra for both PG and NGC (Figure 4c,d) exhibit the same resonance bands at 51 and −103 ppm assigned to Al^{3+} and Si^{4+} in [AlO_4] and [SiO_4], respectively, being well consistent with the results of

DOI: 10.1021/acsami.9b11516
ACS Appl. Mater. Interfaces 2019, 11, 30053–30064

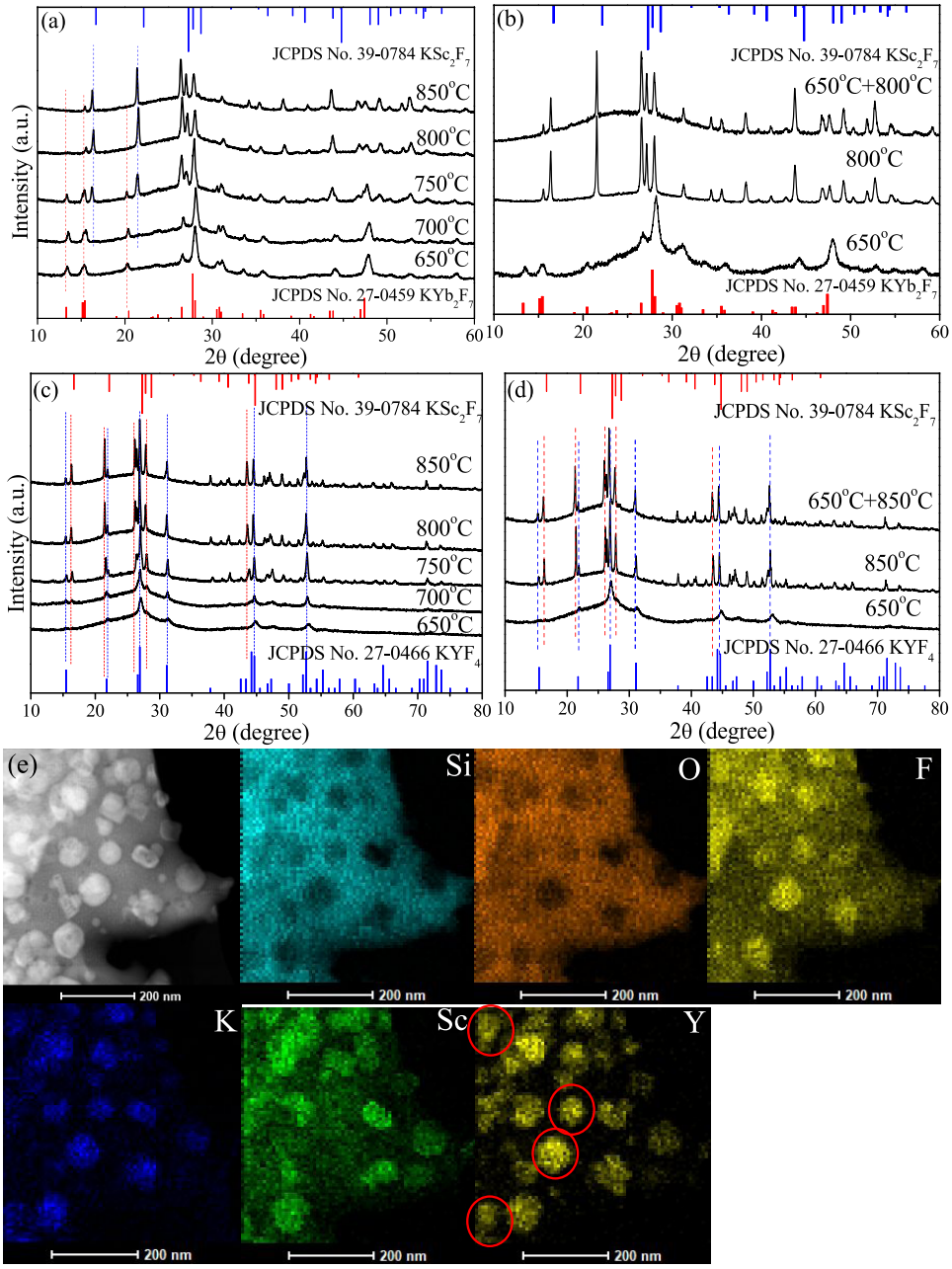

Figure 5. XRD patterns of NGCs with (a) high Yb-to-Sc ratio (3:4) and (c) high Y-to-Sc ratio (3:4) prepared by heating at various temperatures. (b, d) XRD patterns of the corresponding NGCs prepared by directly heating at 650 °C (bottom) and 850 °C (middle) and by reheating the NGC sample (obtained via crystallization at 650 °C) to 850 °C for 2 h (top). (e) STEM-HAADF images of KSc_2F_7 and KYF_4 dual-phase NGC associated with Si (cyan), O (orange), F (yellow), K (blue), Sc (green), and Y (yellow) element mappings. The glass composition (mol %) is $46SiO_2–6Al_2O_3–9K_2CO_3–19KF–16ScF_3–12LnF_3$ (Ln = Yb or Y).

FTIR and Raman spectra. Only one resonance band at 4 ppm is detected in the 45Sc MAS–NMR spectrum of PG, while an extra resonance band of Sc^{3+} at 48 ppm appears for NGC (Figure 4e), which is assigned to Sc in the KSc_2F_7 crystal. Three intense resonance F signals for both PG and NGC are observed in the ^{19}F MAS–NMR spectra (Figure 4f). The resonance at −148 ppm is assigned to fluorine in Al–F–K groups, and the signal intensity significantly reduces after glass crystallization due to the release of F^- ions from these groups to involve in KSc_2F_7 nucleation/growth. The detected F resonance bands at −73 and −183 ppm in NGC are attributed to different bridging fluorine sites in the KSc_2F_7 crystal.[44] For PG, similar F resonance signals at −57 and −179 ppm with a slight blue shift relative to those of NGC are observed, indicating that K/Sc/F-rich amorphous nanodomains may have already formed in glass.

As schematically illustrated in Figure 4g, the network structure of the present oxyfluoride glasses consists of $[SiO_4]$ groups interlinked with $[AlO_4]$ tetrahedra through bridging oxygen atoms. F^- anions will substitute partial O^{2-} ones to enter the glass network followed by the formation of $[AlO_{4-x}F_x]$ units, and K^+, Sc^{3+}, and Ln^{3+} cations act as network modifiers to balance the negative charges of either nonbridging oxygen ions or tetrahedral structure units. In glass, cation field strength, defined as Z/R^2, where Z is the ionic charge and R is the ionic radius) of modifiers increases along

DOI: 10.1021/acsami.9b11516
ACS Appl. Mater. Interfaces 2019, 11, 30053–30064

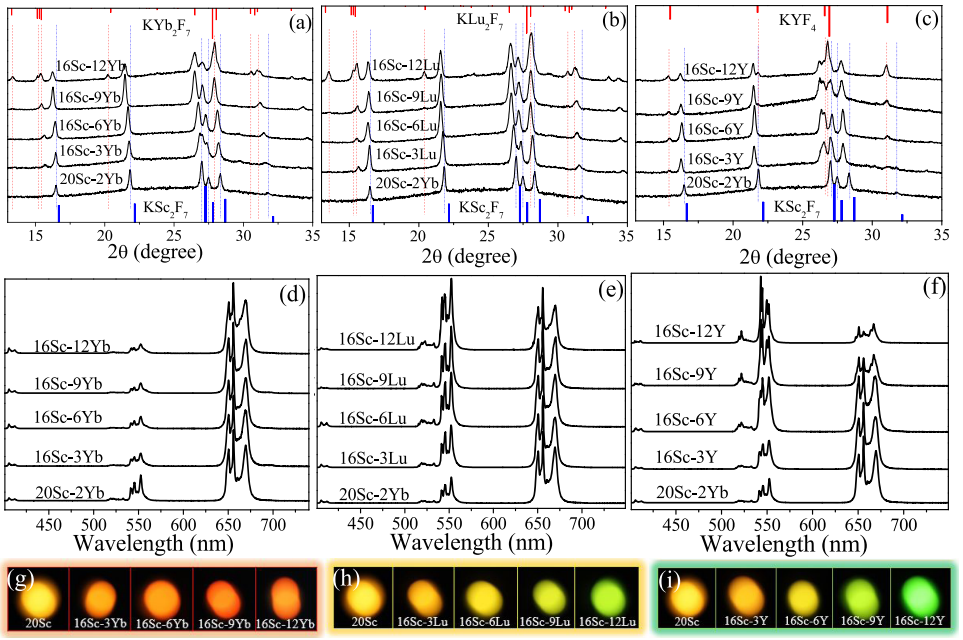

Figure 6. XRD patterns and UC emission spectra for a series of dual-phase NGCs with variation of Ln-to-Sc ratio: (a, d) Ln = Yb, (b, e) Ln = Lu, and (c, f) Ln = Y. (g-i) Multicolor UC luminescence photographs for the corresponding Yb/Er-doped dual-phase NGCs under irradiation of 980 nm laser.

the series K^+ < Ln^{3+} and La^{3+} < Ce^{3+} <.....< Yb^{3+} < Lu^{3+} < Sc^{3+}.[46] Accordingly, the detachment of modifiers from glass network follows the order of K^+ > Ln^{3+} > Sc^{3+}. Therefore, we propose that the K/Ln/F-rich amorphous clusters first separate from glass during melt-quenching and then act as nucleating centers to promote the formation of K/Sc/Ln/F nanodomains (Figure 4g). In fact, molecular dynamics simulations have previously predicted the presence of Na/Ln/F amorphous segregation in the oxyfluoride aluminosilicate glasses.[27,47] When the ionic radius of Ln^{3+} (Ln = Ho−Lu, Y) is small, the nanodomain can accommodate enough Sc^{3+} ions to induce their nucleation/growth and precipitate the $K(Sc/Ln)_2F_7$ crystalline phase from glass via heat treatment (Figure 4h).

Indeed, we observed that the precipitation of orthorhombic KYb_2F_7 or KLu_2F_7 from glass preceded that of orthorhombic KSc_2F_7 when the Ln-to-Sc (Ln = Yb, Lu) ratio in glass was increased up to 3:4 (Figures 5a and S7a). Interestingly, with elevation of crystallization temperature, KLn_2F_7 (Ln = Yb, Lu) NCs first nucleate and grow up and are gradually transformed into KSc_2F_7 NCs. To verify the growth of KSc_2F_7 at the expense of KLn_2F_7, a control experiment by reheating the NGC sample (obtained via crystallization at 650 °C) to 800 °C for 2 h was performed (Figures 5b and S7b). As expected, the nascent KLn_2F_7 NCs are almost consumed and converted into KSc_2F_7 ones, indicating that Yb^{3+} and Lu^{3+} in KLn_2F_7 NCs can be gradually replaced by Sc^{3+} with the increase of heating temperature because of their similar crystal structures (Figure S8). HAADF−STEM micrographs and elemental mappings verify the concurrence of Sc and Ln (Ln = Yb, Lu) signals in both KLn_2F_7 and KSc_2F_7 NCs for the dual-phase fluoride-embedded NGCs (Figure S9 and S10). As shown in Figure S11, characteristic Er^{3+} UC emission signals originating from Er^{3+} in KSc_2F_7 NCs gradually occur, while those attributed to Er^{3+} in KLn_2F_7 NCs disappear, certainly confirming the existence of phase transformation from KLn_2F_7 to KSc_2F_7 via Sc-to-Ln cation exchange in glass during heat treatment. Interestingly, for the Sc−Y system, hexagonal KYF_4 NCs were precipitated first but will not be consumed by subsequent growth of orthorhombic KSc_2F_7 NCs with the increase of crystallization temperature (Figure 5c,d), probably owing to their distinct crystal structures (Figure S12). Evidently, inhomogeneous distribution of Sc and Y signals is clearly discerned in elemental mapping images (Figure 5e), confirming the coexistence of KYF_4 and KSc_2F_7 particles in the glass matrix. No obvious Sc^{3+} signal is found in the KYF_4 NCs, verifying that the Sc-to-Y cation exchange in glass is hard to happen for the different crystal structures between hexagonal KYF_4 and orthorhombic KSc_2F_7. However, all of the KSc_2F_7 NCs contain Y^{3+} ions, further confirming the necessity of Ln-dopant-induced KSc_2F_7 crystallization.

3.4. Tuning UC Luminescence in Dual-Phase NGCs.

Benefiting from selective Ln-dopant-induced (Ln = Ho, Y, Er, Tm, Yb, Lu) KSc_2F_7 crystallization, it is possible to produce dual-phase Sc-based and Ln-based fluoride NCs in glass via competitive crystallization. Herein, Sc−Yb, Sc−Lu, and Sc−Y glass systems were designed and prepared with different Sc-to-Ln ratios, as tabulated in Table S2. After heat treatment at 750 °C for 2 h, KSc_2F_7-KYb_2F_7, KSc_2F_7-KLu_2F_7, and KSc_2F_7-KYF_4 dual-phase embedded NGCs with variable crystal phase ratios can be obtained by simply modifying Yb-to-Sc, Lu-to-Sc, and Y-to-Sc ratios, respectively (Figure 6a−c, Table S2). With the increase of Ln^{3+} content in glass, XRD peaks of orthorhombic KSc_2F_7 phase gradually shift toward low diffraction angles due to the incorporation of more Ln^{3+} ions into the KSc_2F_7 lattice, and extra diffraction peaks assigned to orthorhombic KYb_2F_7, orthorhombic KLu_2F_7, and hexagonal KYF_4 phases become intensified, attributing to the increased crystallization fraction of Ln-based fluorides relative to that of KSc_2F_7 one. For comparison, Sc−Gd glass system with the Sc-to-Gd ratio of 4:3 was prepared and glass crystallization can only produce a cubic KGd_3F_{10} phase instead of the Sc-based and Gd-based dual-phase (Figure S13) since Gd dopants with large ionic radii cannot act as nucleating agents to promote KSc_2F_7 precipitation.

DOI: 10.1021/acsami.9b11516
ACS Appl. Mater. Interfaces 2019, 11, 30053−30064

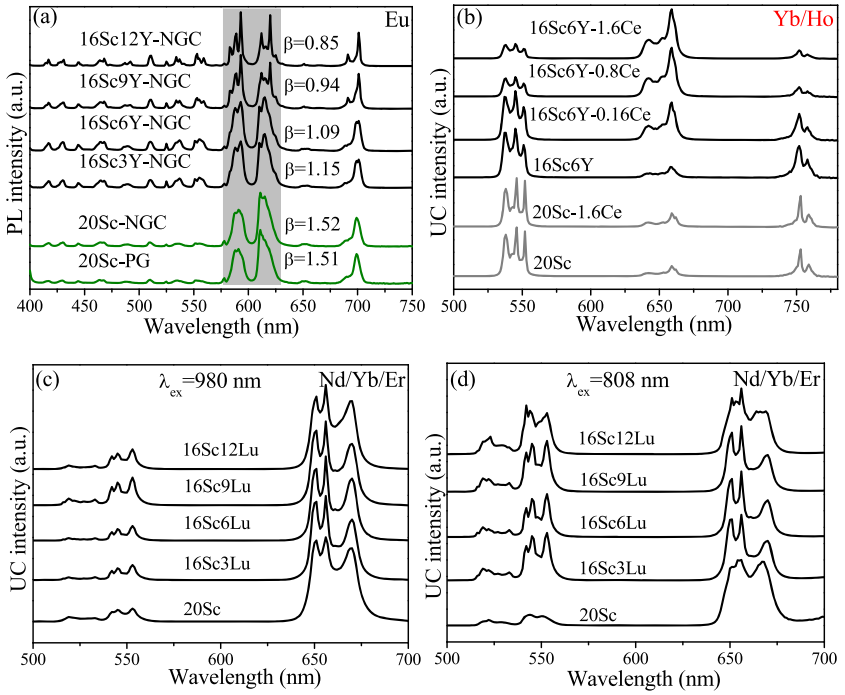

Figure 7. (a) PL spectra of Eu^{3+}-doped 20Sc-PG, 20Sc-NGC, and KSc_2F_7/KYF_4 dual-phase NGCs with various Sc-to-Y ratios. (b) UC spectra of Yb/Ho/Ce tridoped KSc_2F_7 single-phase NGCs and KSc_2F_7/KYF_4 dual-phase NGCs with different Ce^{3+} doping contents. UC emission spectra of Nd/Yb/Er tridoped single-phase NGC and KSc_2F_7/KLu_2F_7 dual-phase NGCs with various Sc-to-Lu ratios under near infrared (NIR) laser excitation: (c) 980 nm laser and (d) 808 nm laser.

In this case, we demonstrate that UC emissive color can be finely tuned via competitive nanocrystallization of Sc-based and Ln-based dual-phase fluorides in glass. Taking Er^{3+} as an emitting activator and Yb^{3+} as a sensitizer, the KSc_2F_7, KYb_2F_7, KLu_2F_7, and KYF_4 single-phase NC-embedded NGC samples show remarkably distinct red-to-green (R/G) UC emission ratios of 3.96, 5.18, 0.79, and 0.47, respectively (Figure S14). A rapid rise in the R/G ratios for Yb/Er:KYF_4, Yb/Er:KLu_2F_7, and Yb/Er:KSc_2F_7 is attributed to the difference in the ionic radii of Y^{3+} (1.04 Å), Lu^{3+} (1.00 Å), and Sc^{3+} (0.89 Å), which results in a gradual decrease of Y−Y, Lu−Lu, and Sc−Sc distances in fluoride lattices. Consequently, Er^{3+} and Yb^{3+} dopants in the KSc_2F_7 lattice by substituting Sc^{3+} ions create closer Yb−Er cation pairs than in the KLu_2F_7 and KYF_4 lattices, leading to high R/G ratio for the Yb/Er:KSc_2F_7 NGC. The highest R/G ratio for the Er:KYb_2F_7 NGC is due to 100% Yb^{3+} content in the crystal host. The corresponding UC emission spectra indicate an obvious enhancement of the *R*/*G* ratio from 3.96 to 10.34 for the Sc−Yb system (Figure 6d and S15), a remarkable decrease of the R/G ratio from 3.96 to 1.07 for the Sc−Lu system (Figures 6e and S15), and the R/G ratio of 0.41 for the Sc−Y system (Figures 6f and S15). The tunability of multicolor UC luminescence for the designed dual-phase NGCs is clearly demonstrated by the change of luminescent photographs (Figure 6g−i) and color coordinates in the Commission International de l'Eclairage (CIE) 1931 chromaticity diagram (Figure S16, Table S3). As far as we know, this is the first report of multicolor UC tuning via controlling dual-phase crystallization in glass.

On the other hand, tuning UC luminescence can also be achieved via selective separation of Ln^{3+} in dual-phase NGCs. As mentioned above, no obvious different change is observed in the Eu^{3+} PL spectra for the Eu^{3+}-doped PG and KSc_2F_7 NGC (Figure 7a) since Eu^{3+} ions do not incorporate into the KSc_2F_7 lattice but stay in the glass matrix after crystallization. However, Eu^{3+} emissive bands become Stark-splitting, decay lifetime is elongated (Figure S17), and emission spectra originating from higher $^5D_{1,2}$ excited states appear in the KSc_2F_7/KYF_4 dual-phase NGCs. Additionally, the integrated intensity ratio between electric dipolar $^5D_0 \rightarrow {}^7F_2$ and magnetic dipolar $^5D_0 \rightarrow {}^7F_1$ transitions gradually decreases from 1.52 to 0.85 with the increase in amount of KYF_4 crystals in NGCs (Figure 7a). All of these results indicate the partition of Eu^{3+} into the KYF_4 crystalline lattice rather than the KSc_2F_7 lattice in the dual-phase NGCs. Consequently, Yb/Ho/Ce tridoped KSc_2F_7/KYF_4 dual-phase NGCs (Figure S18a) were prepared, where Yb/Ho can stay in both KSc_2F_7 and KYF_4 but Ce dopants only locate inside KYF_4. As demonstrated in Figure 7b, introducing Ce^{3+} cannot result in any change of UC color for KSc_2F_7 single-phase NGC but significantly modify UC color from green to red in the dual-phase NGCs. Herein, the obtained dual phases in glass are Yb/Ho:KSc_2F_7 and Yb/Ho/Ce:KYF_4, in which the former produces green UC luminescence and the latter yields red UC luminescence due to the effective cross relaxation between Ce and Ho in KYF_4 (Figure S19).[48,49] The combination of dual-phase UC emissions can result in a tunable green/red UC ratio with variation of Ce doping content. Furthermore, we can achieve incident laser (980 and 808 nm)-dependent UC luminescence by tridoping Nd/Yb/Er in KSc_2F_7/KLu_2F_7 dual-phase NGCs (Figures S18b and 7c,d), where Yb/Er ions partition in both KSc_2F_7 and KLu_2F_7, while Nd ions selectively incorporate in KLu_2F_7 NCs (Figure S20). Upon 980 nm laser excitation (corresponding to Yb^{3+}: $^2F_{7/2} \rightarrow {}^2F_{5/2}$ absorption transition), red UC emission is dominant, indicating that only Er^{3+} in KSc_2F_7 is effectively pumped. This is reasonable since Er UC luminescence in Nd/Yb/Er:KLu_2F_7 NCs will be significantly quenched owing to the detrimental cross relaxation (CR)

DOI: 10.1021/acsami.9b11516
ACS Appl. Mater. Interfaces 2019, 11, 30053−30064

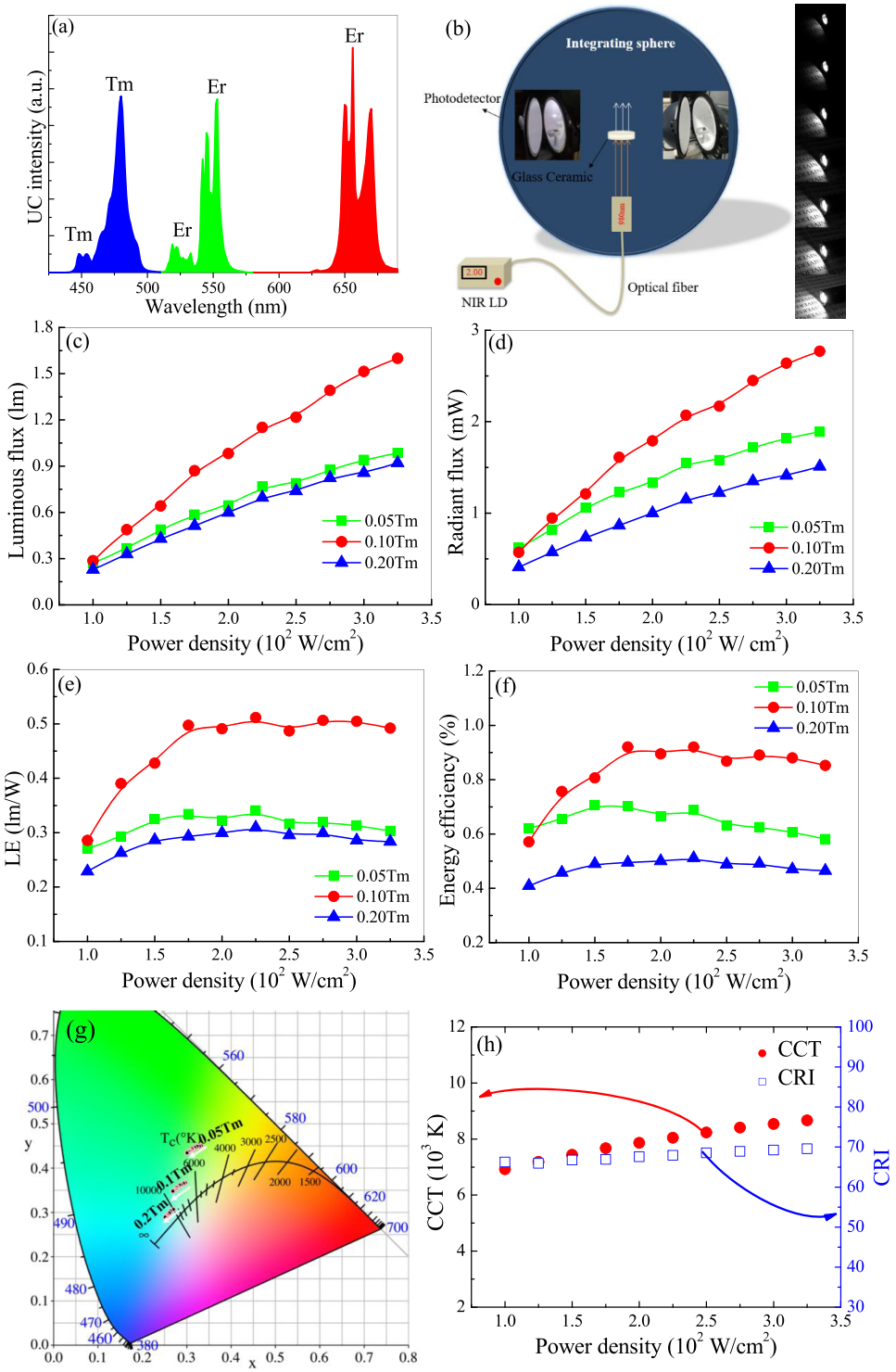

Figure 8. (a) UC emission spectra of Yb/Er/Tm tridoped KSc_2F_7/KLu_2F_7 dual-phase NGCs. (b) Schematic illustration of the measurement system for NIR-laser-driven UC lighting in the transmissive configuration and a dual-phase NGC-based UC lighting device under operation (driven by NIR laser; from top to bottom, laser power density increases). Dependence of (c) luminous flux, (d) radiant flux, (e) LE, and (f) energy efficiency of Yb/Er/Tm (8/0.2/x mol %, x = 0.05, 0.1, 0.2) tridoped NGC-based UC lighting devices on laser power density. (g) Color coordinates and (h) CCT/CRI values versus laser power density for the constructed NIR-laser-driven UC lighting devices.

between Nd^{3+} and Er^{3+} (Figure S21).[50] Upon 808 nm laser excitation (corresponding to Nd^{3+}: $^4I_{9/2} \rightarrow {}^4F_{5/2}$ absorption transition), only Er^{3+} in the KLu_2F_7 host can be effectively excited because of the incorporation of Nd^{3+} sensitizers in KLu_2F_7 NCs and the efficient successive energy transfer from Nd^{3+} to Er^{3+} activators with assistance of Yb^{3+} bridge centers (Figure S21). Notably, the UC emission intensity upon 808 nm laser excitation is far lower than that under 980 nm laser excitation in the present NGCs since Nd ↔ Er CR will significantly depopulate Er^{3+} emitting states.[50]

3.5. Laser-Driven UC Lighting. Laser lighting, currently made of blue laser and downconversion phosphors, is regarded

DOI: 10.1021/acsami.9b11516
ACS Appl. Mater. Interfaces 2019, 11, 30053−30064

as next promising illumination to replace light-emitting diode lighting.[51] However, the irradiation of high-power blue laser will inevitably induce remarkable thermal shock and raise the critical requirement of phosphors and device structures. Recently, we reported that the construction of NIR laser-driven UC solid-state lighting using robust NGCs as a color converter enabled to lessen the thermal attack for the first time.[52] Unfortunately, a stacking structure of Yb/Tm-doped and Yb/Er-doped NGCs is demanded to produce desirable white light. Benefiting from the combined emission spectra from dual-phase NCs in glass, white light UC luminescence can be easily achieved when Yb/Er/Tm are tridoped into the present KSc_2F_7/KLu_2F_7 dual-phase NGCs. As shown in Figure 8a, almost equivalent blue, green, and red (BGR) tricolor UC emission spectra can be obtained in Yb/Er/Tm (8/0.2/0.1 mol %) tridoped KSc_2F_7/KLu_2F_7 dual-phase NGCs with the Sc-to-Lu ratio of 16:6 upon excitation by a 980 nm laser diode (LD). All of these emissions bands can be assigned to $Tm^{3+}/^1D_2 \rightarrow {}^3F_4$ (450 nm), $Tm^{3+}/^1G_4 \rightarrow {}^3H_6$ (480 nm), $Er^{3+}/^2H_{11/2} \rightarrow {}^4I_{15/2}$ (525 nm), $Er^{3+}/^4S_{3/2} \rightarrow {}^4I_{15/2}$ (550 nm), and $Er^{3+}/^4F_{9/2} \rightarrow {}^4I_{15/2}$ (650 nm) transitions (Figure S22).

Herein, as a proof-of-concept experiment, we demonstrated the promising application of the as-prepared dual-phase NGCs as a color converter in NIR laser-driven UC solid-state lighting. The optoelectronic parameters for NGC-based UC lighting under 980 nm laser excitation were systematically evaluated in a transmissive configuration by employing a sphere spectroradiometer system (Figure 8b). The constructed NIR laser-driven UC lighting device produces bright white light, and the brightness significantly enhances with the elevation of incident laser power. The corresponding laser power-dependent UC emission spectra (Figure S23) indicate the improved blue, green, and red tricolor emission spectra. Consequently, both luminous flux and radiant flux of the devices increase with the elevation of laser power density (Figure 8c,d) and the maximal luminous efficiency (LE) and energy efficiency reach about 0.5 Lm/W and 0.9% at a laser power density above 150 W/cm^2, respectively (Figure 8e,f). These optoelectronic parameters for the Yb/Er/Tm (8/0.2/x mol %, x = 0.05, 0.1, 0.2) tridoped dual-phase NGC-based devices are highly dependent on Tm^{3+} concentration, and the optimal Tm^{3+} doping content is 0.1 mol %. As demonstrated in the CIE diagram (Figure 8g), the devices produce green-yellow, white, and cyan luminescence for the 0.05, 0.1, and 0.2 mol % Tm^{3+} doping samples, respectively. Generally, Tm^{3+} blue UC luminescence is three-($^1G_4$) and four-photon ($^1D_2$) absorption processes, while Er^{3+} green/red emission spectra are a two-photon process.[2,19] Therefore, the Tm^{3+} UC intensity shows a more significant increase than the Er^{3+} UC intensity with the increase of laser power density, leading to the slight shifting of color coordinates (Figure 8g) and the increase of correlated color temperature (CCT) from 6900 to 8500 (Figure 8h). Fortunately, the produced lighting from the device fabricated by Yb/Er/Tm (8/0.2/0.1) mol % tridoped NGC falls within the white light region and the corresponding color rendering index (CRI) is about 70 with a gradual increase of laser power density (Figure 8h).

4. CONCLUSIONS

In summary, this study offers a facile route to realize the nucleation/growth of KSc_2F_7 NCs in aluminosilicate glass through Ln^{3+} doping. Small-size Ln^{3+} dopants (Ln = Ho−Lu, Y) act as nucleating agents to promote KSc_2F_7 precipitation from the glass matrix, enabling them easily enter the KSc_2F_7 host by replacing Sc^{3+} ions. Importantly, Sc-based and Ln-based dual-phase fluoride NCs can be simultaneously crystallized in glass via simply modifying the Ln-to-Sc (Ln = Yb, Lu, Y) ratio. Selective separation of Ln^{3+} dopants in dual-phase NGCs enables them to produce finely tunable UC colors with a multichannel access, including changing the dual-phase ratios, Ln^{3+}-emitting centers, and laser excitation wavelengths. Finally, NIR laser-driven UC solid-state lighting with an optimal luminous efficiency of 0.5 lm/W and an energy efficiency of 0.9% is constructed by coupling Yb/Er/Tm-doped dual-phase NGC with 980 nm LD. This work exploits a new way to promote the precipitation of specific crystals in the glass matrix and provides an important advancement in exploring innovative high-performance UC emissive glass ceramic composites.

■ ASSOCIATED CONTENT

Supporting Information

The Supporting Information is available free of charge on the ACS Publications website at DOI: 10.1021/acsami.9b11516.

Extra XRD, HAADF-STEM images, elemental mapping, UC emission spectra, decay curves, and CIE diagrams (PDF)

■ AUTHOR INFORMATION

Corresponding Author

*E-mail: dqchen@fjnu.edu.cn.

ORCID

Daqin Chen: 0000-0003-0088-2480

Author Contributions

‖D.C. and Y.P contributed equally to this work.

Notes

The authors declare no competing financial interest.

■ ACKNOWLEDGMENTS

This research was supported by the National Natural Science Foundation of China (51572065, 51802064) and Zhejiang Provincial Natural Science Foundation of China (LY18E020006).

■ REFERENCES

(1) Auzel, F. Upconversion and Anti-Stokes Processes with f and d Ions in Solids. *Chem. Rev.* **2004**, *104*, 139−172.

(2) Wang, F.; Liu, X. G. Recent Advances in the Chemistry of Lanthanide-Doped Upconversion Nanocrystals. *Chem. Soc. Rev.* **2009**, *38*, 976−989.

(3) Zhou, J. J.; Chen, G. X.; Wu, E.; Bi, G.; Wu, B. T.; Teng, Y.; Zhou, S. F.; Qiu, J. R. Ultrasensitive Polarized Up-Conversion of Tm^{3+}-Yb^{3+} Doped β-$NaYF_4$ Single Nanorod. *Nano Lett.* **2013**, *13*, 2241−2246.

(4) Dong, H.; Sun, L. D.; Yan, C. H. Energy Transfer in Lanthanide Upconversion Studies for Extended Optical Applications. *Chem. Soc. Rev.* **2015**, *44*, 1608−1634.

(5) Yang, D. M.; Ma, P. A.; Hou, Z. Y.; Cheng, Z. Y.; Li, C. X.; Lin, J. Current Advances in Lanthanide Ion (Ln^{3+})-Based Upconversion Nanomaterials for Drug Delivery. *Chem. Soc. Rev.* **2015**, *44*, 1416−1448.

(6) Xu, J. T.; Yang, P. P.; Sun, M. D.; Bi, H. T.; Liu, B.; Yang, D.; Gai, S. L.; He, F.; Lin, J. Highly Emissive Dye-Sensitized Upconversion Nanostructure for Dual-Photosensitizer Photodynamic Therapy and Bioimaging. *ACS Nano* **2017**, *11*, 4133−4144.

DOI: 10.1021/acsami.9b11516
ACS Appl. Mater. Interfaces 2019, 11, 30053−30064

(7) Gu, B.; Zhang, Q. C. Recent Advances on Functionalized Uupconversion Nanoparticles for Detection of Small Molecules and Ions in Biosystems. *Adv. Sci.* **2018**, *5*, No. 1700609.
(8) Zhu, X.; Su, Q.; Feng, W.; Li, F. Y. Anti-Stokes Shift Luminescent Materials for Bio-Applications. *Chem. Soc. Rev.* **2017**, *46*, 1025−1039.
(9) Homann, C.; Krukewit, L.; Frenzel, F.; Grauel, B.; Wurth, C.; Resch-Genger, U.; Haase, M. $NaYF_4$:Yb,Er/$NaYF_4$ Core/Shell Nanocrystals with High Upconversion Luminescence Quantum Yield. *Angew. Chem., Int. Ed.* **2018**, *57*, 8765−8769.
(10) Zhou, B.; Yan, L.; Tao, L. L.; Song, N.; Wu, M.; Wang, T.; Zhang, Q. Y. Enabling Photon Upconversion and Precise Control of Donor-Acceptor Interaction through Interfacial Energy Transfer. *Adv. Sci.* **2018**, *5*, No. 1700667.
(11) Hudry, D.; Howar, I. A.; Popescu, R.; Gerthsen, D.; Richards, B. S. Structure-Property Relationships in Lanthanide-Doped Upconverting Nanocrystals: Recent Advances in Understanding Core-Shell Structures. *Adv. Mater.* **2019**, *31*, No. 1900623.
(12) Wang, F.; Liu, X. G. Upconversion Multicolor Fine-Tuning: Visible to Near-Infrared Emission from Lanthanide-Doped $NaYF_4$ Nanoparticles. *J. Am. Chem. Soc.* **2008**, *130*, 5642−5643.
(13) Heer, S.; Kompe, K.; Gudel, H. U.; Haase, M. Highly Efficient Multicolour Upconversion Emission in Transparent Colloids of Lanthanide-Doped $NaYF_4$ Nanocrystals. *Adv. Mater.* **2004**, *16*, 2102−2105.
(14) Dawson, P.; Romanowski, M. Excitation Modulation of Upconversion Nanoparticles for Switch-Like Control of Ultraviolet Luminescence. *J. Am. Chem. Soc.* **2018**, *140*, 5714−5718.
(15) Cheng, X. W.; Pan, Y.; Yuan, Z.; Wang, X. W.; Su, W. H.; Yi, L. S.; Xie, X. J.; Huang, L. Er^{3+} Sensitized Photon Upconversion Nanocrystals. *Adv. Funct. Mater.* **2018**, *28*, No. 1800208.
(16) Zhou, B.; Shi, B. Y.; Jin, D. Y.; Liu, X. G. Controlling Upconversion Nanocrystals for Emerging Applications. *Nat. Nanotechol.* **2015**, *10*, 924−936.
(17) Zhou, J. J.; Wen, S. H.; Liao, J. Y.; Clarke, C.; Tawfik, S. A.; Ren, W.; Mi, C.; Wang, F.; Jin, D. Y. Activation of the Surface Dark-Layer to Enhance Upconversion in a Thermal Field. *Nat. Photonics* **2018**, *12*, 154−158.
(18) Fischer, S.; Bronstein, N. D.; Swabeck, J. K.; Chan, E. M.; Alivisatos, A. P. Precise Tuning of Surface Quenching for Luminescence Enhancement in Core-Shell Lanthanide-Doped Nanocrystals. *Nano Lett.* **2016**, *16*, 7241−7247.
(19) Liu, Y. S.; Tu, D. T.; Zhu, H. M.; Li, R. F.; Luo, W. Q.; Chen, X. Y. A Strategy to Achieve Efficient Dual-Mode Luminescence of Eu^{3+} in Lanthanides Doped Multifunctional $NaGdF_4$ Nanocrystals. *Adv. Mater.* **2010**, *22*, 3266−3271.
(20) Fischer, S.; Swabeck, J. K.; Alivisatos, A. P. Controlled Isotropic and Anisotropic Shell Growth in β-$NaLnF_4$ Nanocrystals Induced by Precursor Injection Rate. *J. Am. Chem. Soc.* **2017**, *139*, 12325−12332.
(21) Wang, Y.; Zheng, K.; Song, S.; Fan, D.; Zhang, H.; Liu, X. Remote Manipulation of Upconversion Luminescence. *Chem. Soc. Rev.* **2018**, *47*, 6473−6485.
(22) Zhao, J. B.; Zheng, X. L.; Schartner, E. P.; Ionescu, P.; Zhang, R.; Nguyen, T. L.; Jin, D. Y.; Heideprie, H. E. Upconversion Nanocrystal-Doped Glass: a New Paradigm for Photonic Materials. *Adv. Opt. Mater.* **2016**, *4*, 1507−1517.
(23) Pan, Q.; Cai, Z.; Yang, Y.; Yang, D.; Kang, S.; Chen, Z.; Qiu, J.; Zhan, Q.; Dong, G. Engineering Tunable Broadband Near-Infrared Emission in Transparent Rare-Earth Doped Nanocrystals-in-Glass composites via a Bottom-up Strategy. *Adv. Opt. Mater.* **2019**, *7*, No. 1801482.
(24) Liu, X. F.; Zhou, J. J.; Zhou, S. F.; Yue, Y. Z.; Qiu, J. R. Transparent Glass-Ceramics Functionalized by Dispersed Crystals. *Prog. Mater. Sci.* **2018**, *97*, 38−96.
(25) Zhong, J. S.; Chen, D. Q.; Peng, Y. Z.; Lu, Y. D.; Chen, X.; Li, X. Y.; Ji, Z. G. A Review on Nanostructured Glass Ceramics for Promising Application in Optical Thermometry. *J. Alloys Compd.* **2018**, *763*, 34−48.
(26) Chen, D. Q.; Yu, Y. L.; Huang, P.; Lin, H.; Shan, Z. F.; Wang, Y. S. Color-Tunable Luminescence of Eu^{3+} in LaF_3 Embedded Nanocomposite for Light Emitting Diode. *Acta Mater.* **2010**, *58*, 3035−3041.
(27) Li, X. Y.; Chen, D. Q.; Huang, F.; Chang, G. C.; Zhao, J. J.; Qiao, X. S.; Xu, J. C.; Du, X. H.; Yin, M. Phase-Selective Nanocrystallization of $NaLnF_4$ in Aluminosilicate Glass for Random Laser and 940 nm LED-Excitable Upconverted Luminescence. *Laser Photonics Rev.* **2018**, *12*, No. 1800030.
(28) Xu, X. H.; Zhang, W. F.; Yang, D.; Lu, W.; Qi, J. B.; Yu, S. F. Phonon-Assisted Population Inversion in Lanthanide-Doped Upconversion Ba_2LaF_7 Nanocrystals in Glass-Ceramics. *Adv. Mater.* **2016**, *28*, 8045−8050.
(29) Herrmann, A.; Tylkowski, M.; Bocker, C.; Rüssel, C. Cubic and Hexagonal $NaGdF_4$ Crystals Precipitated from an Aluminosilicate Glass: Preparation and Luminescence Properties. *Chem. Mater.* **2013**, *25*, 2878−2884.
(30) Lin, C. G.; Bocker, C.; Rüssel, C. Nanocrystallization in Oxyfluoride Glasses Controlled by Amorphous Phase Separation. *Nano Lett.* **2015**, *15*, 6764−6769.
(31) Fedorov, P. P.; Luginina, A. A.; Popov, A. I. Transparent Oxyfluoride Glass Ceramics. *J. Fluorine Chem.* **2015**, *172*, 22−50.
(32) Zhou, S. F.; Jiang, N.; Miura, K.; Tanabe, S.; Shimizu, M.; Sakakura, M.; Shimotsuma, Y.; Nishi, M.; Qiu, J. R.; Hirao, K. Simultaneous Tailoring of Phase Evolution and Dopant Sistribution in the Glassy Phase for Controllable Luminescence. *J. Am. Chem. Soc.* **2010**, *132*, 17945−17952.
(33) Chen, D. Q.; Wan, Z. Y.; Zhou, Y.; Zhou, X. Z.; Yu, Y. L.; Zhong, J. S.; Ding, M. Y.; Ji, Z. G. Dual-Phase Glass Ceramic: Structure, Dual-Modal Luminescence, and Temperature Sensing Behaviors. *ACS Appl. Mater. Interfaces* **2015**, *7*, 19484−19493.
(34) Chen, D. Q.; Wan, Z. Y.; Liu, S. Highly Sensitive Dual-Phase Nanoglass-Ceramics Self-Calibrated Optical Thermometer. *Anal. Chem.* **2016**, *88*, 4099−4106.
(35) Gao, Z.; Guo, S.; Lu, X. S.; Orava, J.; Wagner, T.; Zheng, L.; Liu, Y.; Sun, S.; He, F.; Yang, P.; Ren, J.; Yang, Y. Controlling Selective Doping and Energy Transfer Between Transition Metal and Rare Earth Ions in Nanostructured Glassy Solids. *Adv. Opt. Mater.* **2018**, *6*, No. 1701407.
(36) Tanabe, S.; Hayashi, H.; Hanada, T.; Onodera, N. Fluorescence Properties of Er^{3+} Ions in Glass Ceramics Containing LaF_3 Nanocrystals. *Opt. Mater.* **2002**, *19*, 343−349.
(37) Chen, D. Q.; Yu, Y. L.; Huang, P.; Weng, F. Y.; Lin, H.; Wang, Y. S. Optical Spectroscopy of Eu^{3+} and Tb^{3+} Doped Glass Ceramics Containing $LiYbF_4$ Nanocrystals. *Appl. Phys. Lett.* **2009**, *94*, No. 041909.
(38) de Pablos-Martin, A.; Ramirez, M. O.; Duran, A.; Bausa, L. E.; Pascual, M. J. Tm^{3+} Doped Oxy-Fluoride Glass-Ceramics Containing $NaLaF_4$ Nano-Crystals. *Opt. Mater.* **2010**, *33*, 180−185.
(39) Cao, J. K.; Wang, X.; Li, X. M.; Wei, Y. L.; Chen, L. P.; Guo, H. Enhanced Emissions in Tb^{3+}-Doped Oxyfluoride Scintillating Glass Ceramics Containing KLu_2F_7 Nano-Crystals. *J. Lumin.* **2016**, *170*, 207−211.
(40) Zhang, W. J.; Chen, Q. J.; Zhang, Q. Y.; Jiang, Z. H. Enhanced 2.0 μm Emission in Oxyfluoride Glass-Ceramics Containing Nanocrystals MF_2 (MF_3): Ho^{3+},Tm^{3+} (M = Ca, Ba, and La). *J. Non-Cryst. Solids* **2011**, *357*, 2278−2281.
(41) Li, X. M.; Cao, J. K.; Wei, Y. L.; Yang, Z. R.; Guo, H. Optical Thermometry Based on Up-Conversion Luminescence Behavior of Er^{3+}-Doped Transparent Sr_2YbF_7 Glass-Ceramics. *J. Am. Ceram. Soc.* **2015**, *98*, 3824−3830.
(42) Teng, X.; Zhu, Y.; Wei, W.; Wang, S.; Huang, J.; Naccache, R.; Hu, W.; Tok, A. I. Y.; Han, Y.; Zhang, Q.; Fan, Q.; Huang, W.; Capobianco, J. A.; Huang, L. Lanthanide-Doped Na_xScF_{3+x} Nanocrystals: Crystal Structure Evolution and Multicolor Tuning. *J. Am. Chem. Soc.* **2012**, *134*, 8340−8343.
(43) Chen, D. Q.; Peng, Y. Z.; Li, X. Y.; Zhong, J. S.; Huang, P. Competitive Nanocrystallization of Na_3ScF_6 and $NaYbF_4$ in

DOI: 10.1021/acsami.9b11516
ACS Appl. Mater. Interfaces 2019, 11, 30053−30064

Aluminosilicate Glass and Optical Spectroscopy of Ln^{3+} Dopants. *Ceram. Int.* **2018**, *44*, 15666−15673.
(44) Rakhmatullin, A.; Polovov, I. B.; Maltsev, D.; Alix, M.; Volkovich, V.; Chukin, A. V.; Boca, M.; Bessada, C. Combined Approach for the Structural Characterization of Alkali Fluoroscandates: Solid-State NMR, Powder X-ray Diffraction, and Density Functional Theory Calculations. *Inorg. Chem.* **2018**, *57*, 1184−1195.
(45) Goel, A.; Tulyaganov, D. U.; Kharton, V. V.; Yaremchenko, A. A.; Erilsson, S.; Ferreira, J. M. F. Optimization of La_2O_3-Containing Diopside Based Glass-Ceramic Sealants for Fuel Cell Applications. *J. Power Sources* **2009**, *189*, 1032−1043.
(46) Iftekhar, S.; Pahari, B.; Okhotnikov, K.; Jaworski, A.; Stevensson, B.; Grins, J.; Eden, M. Properties and Structures of RE_2O_3-Al_2O_3-SiO_2 (RE = Y, Lu) Glasses Probed by Molecular Dynamics Simulations and Solid-State NMR: The Roles of Aluminum and Rare-Earth Ions for Dictating the Microhardness. *J. Phys. Chem. C* **2012**, *116*, 18394−18406.
(47) Peng, Y. Z.; Zhong, J. S.; Li, X. Y.; Chen, J. K.; Zhao, J. J.; Qiao, X. V.; Chen, D. Q. Controllable Competitive Nanocrystallization of La^{3+}-Based Fluorides in Aluminosilicate Glasses and Optical Spectroscopy. *J. Eur. Ceram. Soc.* **2019**, *39*, 1420−1427.
(48) Chen, G. Y.; Liu, H. C.; Somesfalean, G.; Liang, H. J.; Zhang, Z. G. Upconversion Emission Tuning from Green to Red in Yb^{3+}/Ho^{3+}-Codoped $NaYF_4$ Nanocrystals by Tridoping with Ce^{3+} Ions. *Nanotechnology* **2009**, *20*, No. 385704.
(49) Chen, D. Q.; Liu, L.; Huang, P.; Ding, M. Y.; Zhong, J. S.; Ji, Z. G. Nd^{3+}-Sensitized Ho^{3+} Single-Band Red Upconversion Luminescence in Core-Shell Nanoarchitecture. *J. Phys. Chem. Lett.* **2015**, *6*, 2833−2840.
(50) Xie, X. J.; Gao, N. Y.; Deng, R. R.; Sun, Q.; Xu, Q. H.; Liu, X. G. Mechanistic Investigation of Photon Upconversion in Nd^{3+}-Sensitized Core-Shell Nanoparticles. *J. Am. Chem. Soc.* **2013**, *135*, 12608−12611.
(51) Li, S. X.; Wang, L.; Hirosaki, N.; Xie, R. J. Color Conversion Materials for High-Brightness Laser-Driven Solid-State Lighting. *Laser Photonics Rev.* **2018**, *12*, No. 1800173.
(52) Chen, J. K.; Peng, Y. Z.; Li, X. Y.; Chen, W.; Huang, H.; Lin, L.; Chen, D. Q. Near-Infrared-Laser-Driven Robust Glass Ceramic Based Upconverted Solid-State-Lighting. *J. Mater. Chem. C* **2019**, *7*, 4109−4117.

DOI: 10.1021/acsami.9b11516
ACS Appl. Mater. Interfaces 2019, 11, 30053−30064